STIFFNESS PREDICTION AND VALIDATION OF LARGE VOLUME 3D PRINTED, SHORT-FIBER-FILLED POLYMER COMPOSITES

Timothy Russell and David A. Jack

Baylor University
Waco, Texas

ABSTRACT

Large-volume 3D deposition of short carbon fiber filled (CFF) thermoplastic composites greatly enhances the value and potential of additive manufacturing by offering fast production of large-scale tooling and even large-scale, end-use parts. Validated models to predict the material properties as a function of processing parameters of such 3D printed composites aid in driving down the design cost of a production part by eliminating the need to process large volumes of material in trial prints and the subsequent final product characterization. In this study, a method of predicting the effective elastic modulus from the flow simulation to the final deposition and cooling of a short fiber filled deposited structure is presented. Specifically, a 13% CFF acrylonitrile butadiene styrene (ABS) is considered. An in-house, large volume 3D printer was built and used to print tensile bars that were tested based off ASTM-D3039. Modeling was carried out using a custom MATLAB code to model the fiber orientation state along the velocity field streamlines within the nozzle, the die-swell of the extrudate, and the subsequent deposition onto the moving platen. The resulting predicted fiber orientation state is then coupled with micromechanical modeling to obtain a spatially varying anisotropic stiffness tensor. This result is then used within a finite element model with spatial varying stiffness to mimic the effective stiffness of the processed composite. Modeling results indicate little difference between a fully filled deposition (i.e., no interlaminar voids between deposition beads) and the actual cross-sectioned geometry. The results obtained from the RSC fiber interaction model for a value of $\kappa = 1/30$ and $C_I = 0.03$ were in the best agreement with the experimental testing with a differential of less than 20% between experiment and modeling, and future work will be required to better characterize the flow parameters before the modeling efforts can be considered fully validated.

1. INTRODUCTION

Among the many advancements the 3D printing industry has made over recent decades is large area additive manufacturing (LAAM). LAAM has the potential to produce large-scale tooling and large-scale, end-use parts. For example, Oak Ridge National Laboratories, in partnership with TPI Composites, used a LAAM variant that they termed the BAAM (Big Area Additive Manufacturing) to print a mold for a 13 m wind turbine in only eight segments [1]. In addition, Oak Ridge has shown their ability to print large functional parts such as the chassis for a Shelby Cobra using a 20% CFF ABS [2,3]. Whether a mold or an end-use part is desired to be made using LAAM, it is desirable to be able to predict the resulting anisotropic mechanical properties of the parts before they are printed. Doing so could lessen the need for trial-and-error

Copyright 2019. Used by the Society of the Advancement of Material and Process Engineering with permission.

SAMPE Conference Proceedings. Charlotte, NC, May 20-23, 2019. Society for the Advancement of Material and Process Engineering – North America.

printing to determine what a part's capabilities are and aid in materials selection for the desired application. Thus, accurate prediction of the anisotropic mechanical properties of LAAM-made, short fiber composite parts could accelerate the design phase of LAAM manufacturing.

To predict the anisotropic mechanical properties of a 3D printed, short-fiber composite part, knowledge of the internal, spatially varying fiber orientation state is required. Jeffery modeled the motion of a single, rigid, massless, ellipsoidal fiber in 1922 [4]. Folgar and Tucker in 1984 [5] introduced an Isotropic Rotary Diffusion (IRD) model, which is commonly used in the present day within the injection molding industry [6]. In recent years, the Reduced Strain Closure (RSC) [7] and similar forms such as the SRF [8] have expanded upon the usefulness of the IRD model to better represent the transient orientation state within a polymer melt. 3D printing, although similar to that of a closed mold process within the deposition nozzle, experiences a swell of the extrudate upon the exiting of the nozzle. The present authors in Russell *et al.* [9] demonstrated the ability to model the orientation state within the nozzle through to deposition, but did not compare their results to that from experimental testing. LAAM is a relatively new manufacturing technique and little literature has been published on modeling the fiber orientation state in 3D printed composites.

We seek to look at the fiber orientation modeling problem in the context of large-scale Fused Filament Fabrication (FFF). FFF is one of the most common types of 3D printing and involves extruding a molten polymer through a nozzle onto a build plate. The FFF process is distinctly different from injection molding since the processed polymer is exposed to air before being deposited and cooled rather than undergoing long shearing flows inside an injection mold and then being frozen in place inside the mold. Specifically, in the present paper we seek to model the fiber orientation state from manufacturing to the final tensile testing of the processed structure. The structure is made of a carbon fiber reinforced ABS and the predicted elastic modulus, which is dependent on the orientation state, is compared to that of the experimentally characterized elastic modulus of a carbon fiber reinforced ABS tensile bar. The fabricated samples were made using an in-house designed and fabricated LAAM system.

1.1 Fiber Orientation Modeling

We use the IRD and the Reduced Strain Closure (RSC) model by Wang *et al.* [7] for our fiber orientation modeling. The RSC model is an adjusted form of the IRD model that includes a coordinate system invariant slowness parameter to improve the transient orientation state prediction [7]. The IRD and RSC models can be given in terms of orientation tensors as in Equations 1 and 2, respectively:

$$\frac{\mathrm{D}\mathbf{A}}{\mathrm{Dt}} = -\frac{1}{2}(\mathbf{\Omega}\cdot\mathbf{A}-\mathbf{A}\cdot\mathbf{\Omega}) + \frac{1}{2}\lambda(\mathbf{\Gamma}\cdot\mathbf{A}+\mathbf{A}\cdot\mathbf{\Gamma}-2\mathbf{A_4}\colon\mathbf{\Gamma}) + 2C_I\dot{\gamma}(\mathbf{I}-3\mathbf{A}) \tag{1}$$

$$\frac{\mathrm{D}\mathbf{A}}{\mathrm{Dt}} = -\frac{1}{2}(\mathbf{\Omega}\cdot\mathbf{A}-\mathbf{A}\cdot\mathbf{\Omega}) + \frac{1}{2}\lambda\{\mathbf{\Gamma}\cdot\mathbf{A}+\mathbf{A}\cdot\mathbf{\Gamma}-2\mathbf{\Gamma}[\mathbf{A_4}+(1-\kappa)(\mathbf{L_4}-\mathbf{M_4}\colon\mathbf{A_4})]\} + 2\kappa C_I\dot{\gamma}(\mathbf{I}-3\mathbf{A}) \tag{2}$$

In these equations, $\mathbf{A}$ and $\mathbf{A_4}$ are the second and fourth order orientation tensors, respectively; $\mathbf{\Omega}$ is the vorticity tensor; $\mathbf{\Gamma}$ is the rate of deformation tensor; $\lambda = \frac{r_e^2-1}{r_e^2+1}$ takes into account the fiber geometry where r_e is the equivalent ellipsoidal aspect ratio; C_I is the fiber interaction coefficient; $\dot{\gamma}$ is the magnitude of $\mathbf{\Gamma}$; $\mathbf{L_4} = \sum_{i=1}^{3}\lambda_i\boldsymbol{e}_i\boldsymbol{e}_i\boldsymbol{e}_i\boldsymbol{e}_i$ and $\mathbf{M_4} = \sum_{i=1}^{3}\boldsymbol{e}_i\boldsymbol{e}_i\boldsymbol{e}_i\boldsymbol{e}_i$ are constructed from the i-th eigenvalue and eigenvector of $\mathbf{A}$ being λ_i and $\boldsymbol{e}_i$, respectively; and κ is the RSC slowness parameter. Note that Equation 2 will reduce to Equation 1 when $\kappa = 1$.

The IRD and RSC models in Equations 1 and 2 describe the change in the orientation state of a population of suspended fibers over time. We quantify the orientation state of a population of suspended fibers using orientation tensors – specifically $\mathbf{A}$ and $\mathbf{A_4}$. In simple terms, the diagonal components of $\mathbf{A}$, namely A_{11}, A_{22}, and A_{33}, are quantifiers of the fiber alignment in the x_1, x_2, and x_3 directions, respectively. They also obey the property $A_{11} + A_{22} + A_{33} = 1$. Orientation tensors are dependent on the more general fiber orientation probability distribution function but are a more compact and computationally efficient description of the orientation state [10]. It is also important to note that one of our main interests is to predict the fourth order stiffness tensor which requires orientation information that can be extracted from $\mathbf{A_4}$, which contains $\mathbf{A}$, instead of the full probability distribution function [10]. That being said, the anisotropic, homogenized fourth order stiffness tensor can be cast as

$$\begin{aligned}\langle C_{ijkl}\rangle = {} & B_1 A_{ijkl} + B_2\left(A_{ij}\delta_{kl} + A_{kl}\delta_{ij}\right) + B_3\left(A_{ik}\delta_{jl} + A_{il}\delta_{jk}\delta_{jl} + A_{jl}\delta_{ik}\delta_{jl} + A_{jk}\delta_{il}\right) \\ & + B_4\left(\delta_{ij}\delta_{kl}\right) + B_5(\delta_{ik}\delta_{jl} + \delta_{il}\delta_{jk})\end{aligned} \tag{3}$$

where A_{ij} and A_{ijkl} are the (i,j) and (i,j,k,l) components of $\mathbf{A}$ and $\mathbf{A_4}$, respectively, and δ_{ij} is the Kronecker delta [10]. The B_i's in Equation 3 are functions of the transversely isotropic stiffness [10], which is found using the micromechanics model by Tandon and Weng [11]:

$$\begin{aligned} B_1 &= \overline{C}_{1111} + \overline{C}_{2222} - 2\overline{C}_{1122} - 4\overline{C}_{1212} & B_4 &= \overline{C}_{2233} \\ B_2 &= \overline{C}_{1122} - \overline{C}_{2233} & B_5 &= 0.5(\overline{C}_{2222} + \overline{C}_{2233}) \\ B_3 &= \overline{C}_{1212} + 0.5(\overline{C}_{2233} - 2\overline{C}_{2222}) \end{aligned} \tag{4}$$

Finally, throughout this study we let $\mathbf{A} \approx f(\mathbf{A_4})$ using the orthotropic closure [12] in the form introduced by VerWeyst [13].

1.2 Baylor's LAAM System

Baylor's LAAM System, pictured in Figure 1, was assembled in-house and used to print the tensile bars for the experimental study. The cold-rolled steel rails, ¼" aluminum build plate, and 3" tubing that make up the main structure of the system were bought locally, and the tubing was cut and welded together in-house. The system is operated by three unconnected sets of controls, those that control the gantry system, the extruder, and the heated bed. Although these three control systems are independent and can be operated in any order, a general process for operating them is the following: (1) turn on the extruder system, specify its screw RPMs and temperatures and make sure an air hose (for cooling) is attached to it; (2) turn on the gantry system and open its controlling software on the nearby computer; (3) turn on the heated bed and specify its temperature; (4) print a part by commanding the extruder to start extruding and the gantry system to start moving. More details on the three main control systems are given next.

1.2.1 Gantry System

The gantry system, a Magnum II, was obtained from Precision Plasma LLC [14] and was designed for build-it-yourself CNC plasma cutting systems. However, its' 3-axis movement capabilities make it perfectly suitable for our system as well. The gantry system included the aluminum track which is attached to the top cross bar, the side pieces that support the cross bar, and the motors, racks, and pinions. The gantry system is operated from a nearby computer using Mach3 software which takes G-Code input. Thus, the print path for the tensile bars was written in G-Code. Figure 2 shows the Mach3 software interface.

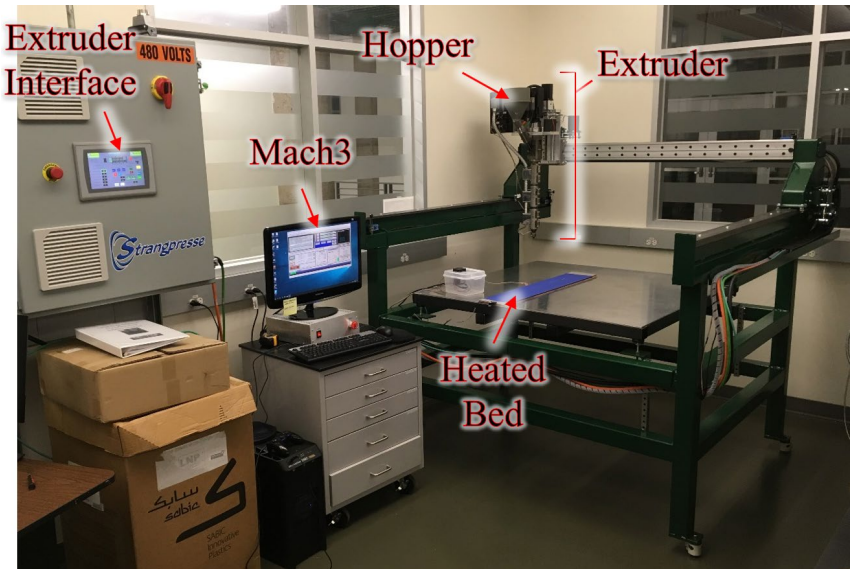


Figure 1. LAAM system at Baylor.

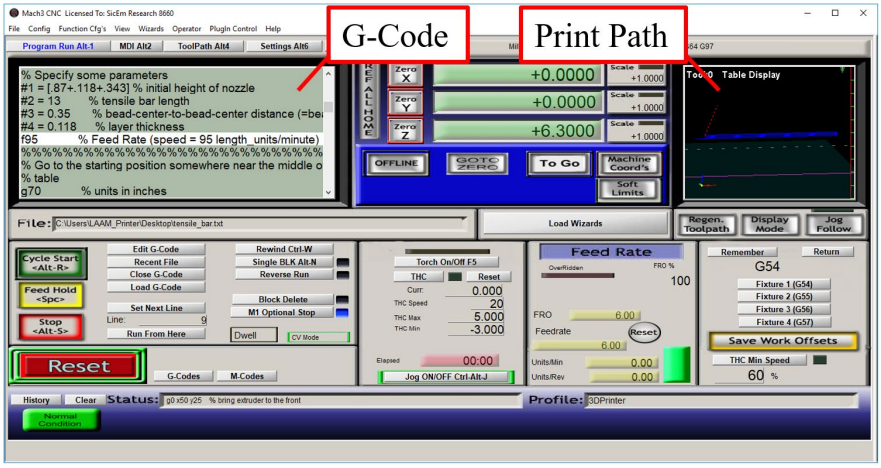


Figure 2. Mach3 software interface.

1.2.2 Extruder

The extruder used in the LAAM system is a Strangpresse Extruder Model 19 [15]. A hopper was made in-house for this extruder and takes in polymer pellets as opposed to polymer filament like most desktop extrusion 3D printers. This makes the extruder more energy and cost effective as most raw polymers are prevalent commercially in pellet form and there is no need to process them into filament with a specified, consistent diameter. The extruder interface is shown in Figure 3 and allows one to adjust the screw RPMs (to control the extrusion rate) and temperatures of the extruder's three temperature zones (also shown in Figure 3). An air tube was also attached to a spigot at the top of the extruder to cool the extruder and mitigate clogging of softened polymer pellets.

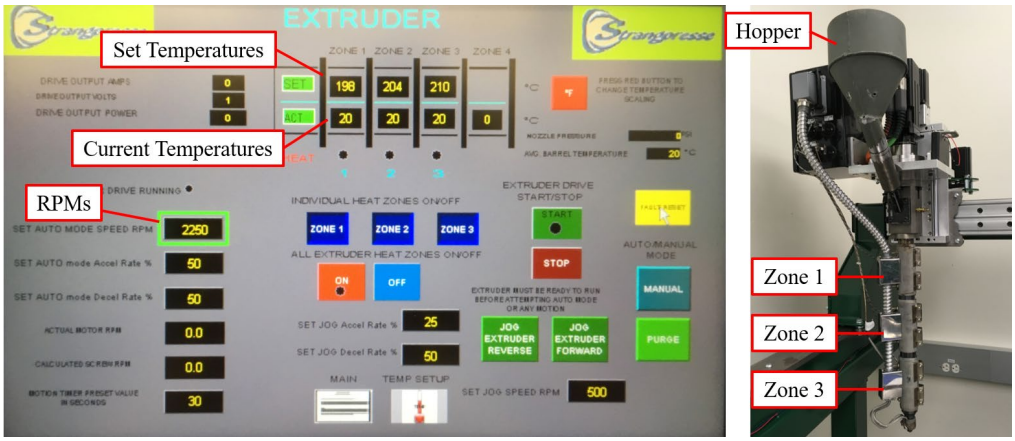


Figure 3. Strangpresse extruder interface (left) and Strangpresse extruder (right).

1.2.3 Heated Bed

Heating the build area of the system helps prevent parts from warping as they are being printed. The heated sheet was sandwiched between a cork board and the aluminum build plate. The tensile bars were printed on the aluminum build plate covered in blue painters' tape (see Figure 1 and Figure 8) to help the printed material adhere better during printing. A temperature controller with a thermocouple was used to measure the temperature of the build plate and adjust it to match the user-specified temperature. In the present study, a heated pad of dimensions 6" x 3' was sufficient for the tensile bars.

2. COMPUTATIONAL METHODOLOGY

We present the computational work in three main steps. The first was to model the nozzle flow in COMSOL using a 2D, planar flow model for both the cavity flow in the nozzle and the stress-free surface of the die swell region and subsequent deposition. Next, custom designed MATLAB codes applying Equations 1 and 2 (the IRD and RSC models) were executed to predict the fiber orientation state in the flow domain and, subsequently, the resulting spatially varying anisotropic stiffness of the deposited bead. The third step was to create a tensile sample geometry in COMSOL and extrapolate the predicted bulk stiffness through the width of each of the beads that make up the tensile sample. This third step was done for a sample with a realistic cross-section and one with an ideal, rectangular cross-section made from rectangular beads. A brief overview of the computational process is shown in Figure 4 and more details on the three steps are given in the following subsections. We also briefly discuss the effects of changing fiber orientation model parameters.

2.1 Flow Modeling

The nozzle flow was modeled in COMSOL as a 2D planar, Newtonian, isothermal, Stokes flow, independent of the orientation state and with the die swell shape creating the zero stress die-swell boundary generated by the method of Heller *et al.* [16,17]. The model domain is shown in Figure 5. The dimensions of the confined flow model region are similar to the actual Strangpresse extruder nozzle and the boundary conditions consisted of the following: the inlet

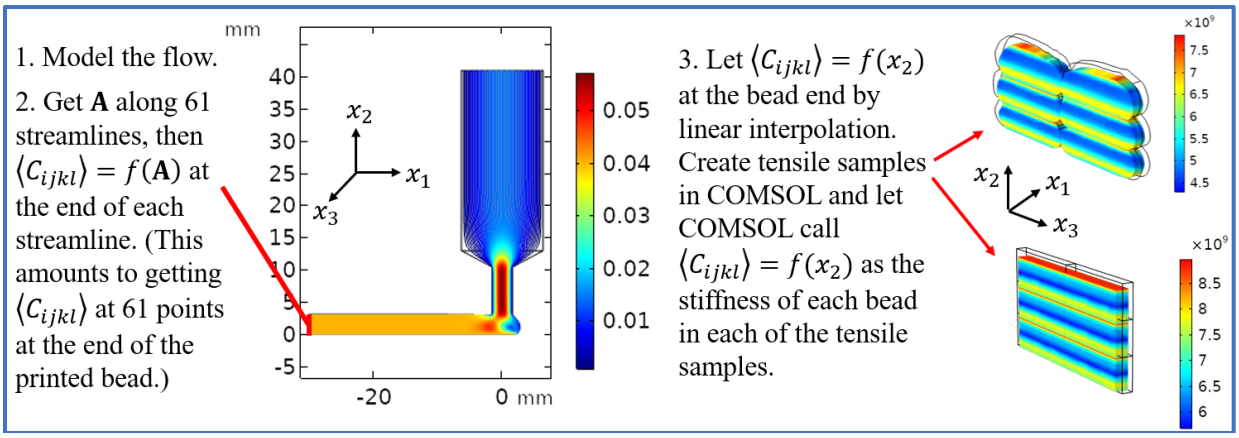


Figure 4. Computational process overview: flow model with color depicting velocity magnitude (left) and tensile samples with color depicting von Mises stress (right).

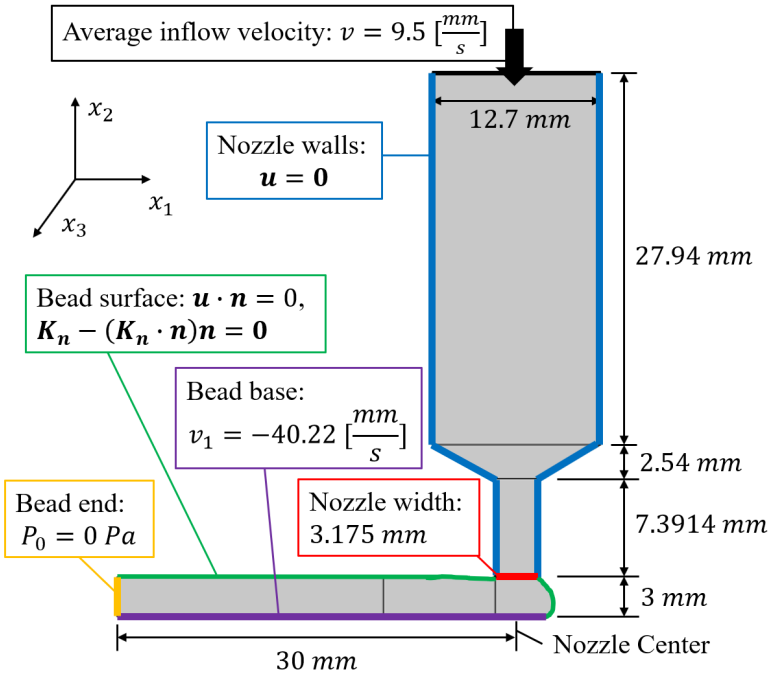


Figure 5. COMSOL nozzle flow model with dimensions and boundary conditions.

average velocity was 9.5 mm/s; the nozzle walls were considered to be no-slip; the exposed part of the bead was considered to be a slip wall; the speed of the base of the bead relative to the nozzle was 40.22 mm/s (95 in/min) in the $-x_1$ direction; the end of the bead (at the far left in Figure 5) was considered a zero pressure outlet. The boundary condition equations and nozzle dimensions are given in Figure 5. The finite element analysis was done with a mesh of over 16,000 elements and the velocities (v_1 and v_2) and velocity gradients ($\frac{\partial v_1}{\partial x_1}$, $\frac{\partial v_2}{\partial x_1}$, $\frac{\partial v_1}{\partial x_2}$, and $\frac{\partial v_2}{\partial x_2}$) were found at discrete points along 61 streamlines in the flow model.

2.2 Orientation Modeling

Once the velocity profile is defined, the orientation state, **A,** is predicted using a custom code to evaluate Equations 1 and 2 in MATLAB with the IRD and RSC fiber interaction models. An isotropic initial orientation state condition was used at the top of the nozzle domain. An isotropic orientation state is defined as $\mathbf{A_o} = 1/3 \cdot \mathbf{I}$, where **I** is the second order identity tensor. The anisotropic, homogenized stiffness tensor $\langle C_{ijkl} \rangle$ is then predicted as a function of **A** at the bead end shown in Figure 5 using Equation 3. In accordance with the number of streamlines used in the flow model, this amounted to getting $\langle C_{ijkl} \rangle$ at 61 points through the thickness of the bead at the bead end. Linear interpolation was used so that each component of $\langle C_{ijkl} \rangle$ could be cast as a continuous function of x_2 and imported into COMSOL to define the properties of a tensile sample. This will be further discussed in subsection 2.3.

The material properties used for the stiffness computations are given in Table 1. The ABS and CF subscripts in Table 1 denote properties of the matrix and fiber, respectively; E is for elastic modulus; ν is for Poisson's ratio; ρ is for density; w_f is for weight fraction; v_f is for volume fraction; a_r is for geometric fiber aspect ratio (i.e. the ratio of length to diameter of the cylindrical fiber); and r_e is for the equivalent ellipsoidal aspect ratio.

Table 1. Material Properties.

Fiber Properties	Matrix Properties
$E_{CF} = 230\ GPa$	$E_{ABS} = 2.25\ GPa$
$\nu_{CF} = 0.2$	$\nu_{ABS} = 0.35$
$\rho_{ABS} = 1700\ kg/m\text{^}3$	$\rho_{ABS} = 1040\ kg/m\text{^}3$
$w_f = 0.13 \rightarrow v_f = \frac{w_f}{w_f + (1-w_f) * \rho_{CF}/\rho_{ABS}} \approx 0.0838$	
$a_r = 20 \rightarrow r_e = 0.000035a_r^3 - 0.00467a_r^2 + 0.764a_r + 0.404$	
≈ 14.1 (see e.g. [18])	

The fibers in the models used in this study are considered to be rigid, cylindrical, and of uniform aspect ratio and distribution. In addition, both the fibers and the polymer matrix are modeled as isotropic, linear elastic materials and considered to be well-bonded (i.e. $\boldsymbol{u}_{CF} = \boldsymbol{u}_{ABS}$ along their interface) in the micromechanics models.

2.3 Tensile Test Simulation

The first step in simulating a tensile test involved taking a photograph of the cross-section of one of our experimental tensile bars, the details of which are discussed in subsection 3.1. These tensile bars, which were two beads wide and three beads tall, were photographed with an iPhone SE (model A1662) and a representative image is shown in Figure 6(a). A MATLAB program was then used that allows a user to open the cross-section photograph on a computer and capture coordinate data point-by-point by manually performing mouse-clicks around the perimeter of the cross-section and voids to trace the boundaries of the deposited beads (see Figure 6(b)). The tensile bar's width and thickness were measured with calipers and input into the program to scale the pixel locations to the physical dimensions of the sample.

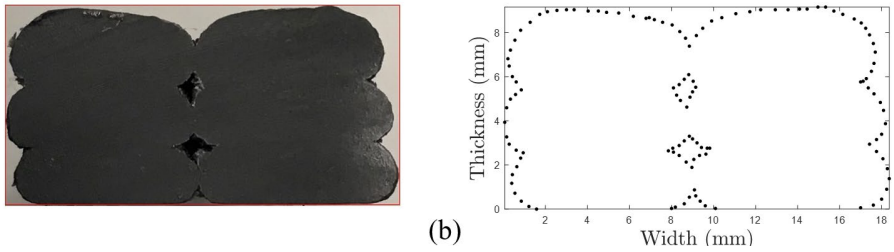


Figure 6. Tensile bar cross-section: (a) photograph and (b) captured points used to define the cross-section for the COMSOL model geometry.

The generated coordinate data was then uploaded in COMSOL to produce a cross-section which was extruded 1 mm to generate the tensile sample geometry shown in Figure 7. We did not model the full 152.4 mm of the tensile bar because it does not affect the elastic modulus prediction and with a shorter model the higher refinement of meshing is allowed to improve the accuracy of the solution. The boundary conditions for the tensile sample (see Figure 7) consisted of fixing the entire back side of the sample in the x_1 direction and displacing the entire front side 1 mm in the $-x_1$ direction. In addition, a point near the center of the backside base was fixed in all directions and another on the left side of the backside base was fixed solely in the x_2 direction to prevent rotation.

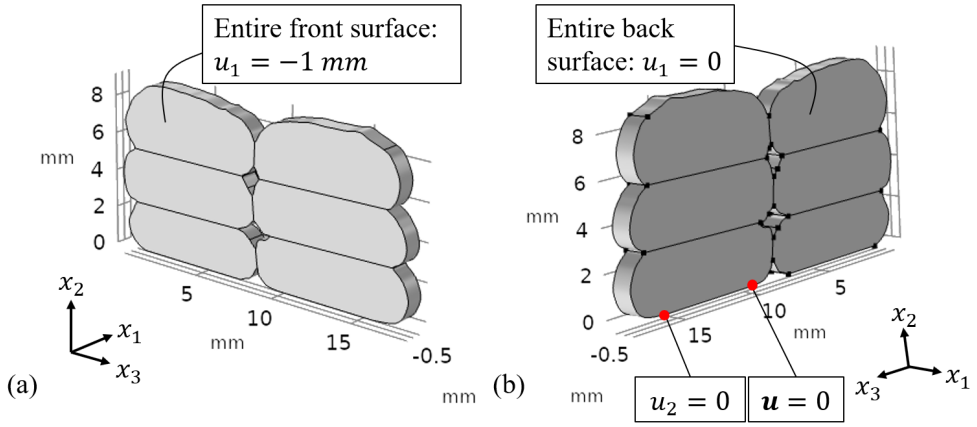


Figure 7. Tensile sample geometry with boundary conditions: (a) front view and (b) back view.

A rectangular tensile bar geometry with the same width and thickness dimensions and similar boundary conditions was also created so that the results from the two models could be compared (see Figure 4). This second modeling scenario is similar to the assumption that the deposited beads fully fill the volume without any voids between the bead paths. Furthermore, in a real tensile sample the beads were not all exactly 3 mm tall. Thus, the $\langle C_{ijkl} \rangle$ that was found as a function of x_2 over the domain $0 \leq x_2 \leq 3$ mm (for the 3 mm bead shown in Figure 5) was linearly mapped to the domain $0 \leq x_2 \leq h$, where h is an actual bead height. This linear mapping was done for each bead in both models. The tensile simulation results are revealed in Table 2 for both models and varying values of C_I and κ which appear in the fiber orientation models.

Table 2. Predicted Effective Longitudinal Modulus (E_1) of a 13 wt% CFF ABS Tensile Bar.

	C_I	κ	Rectangular Cross-Section Geometry	Traced Cross-Section Geometry
IRD	0.01	-	6.87 (GPa)	6.82 (GPa)
	0.03	-	5.60 (GPa)	5.55 (GPa)
RSC	0.01	1/10	4.83 (GPa)	4.70 (GPa)
	0.01	1/30	4.14 (GPa)	4.07 (GPa)
	0.03	1/10	4.68 (GPa)	4.58 (GPa)
	0.03	1/30	4.12 (GPa)	4.05 (GPa)

Table 2 shows that there is a very noticeable difference between the E_1 predictions given by the IRD model and those given by the RSC model, but there is not as much discrepancy due to changing the tensile sample geometry. To confirm these observations, we calculate the percent relative difference (PRD) between two values using

$$PRD = \frac{|value_1 - value_2|}{|value_1 + value_2|/2} \times 100\% \tag{5}$$

The greatest PRD between the IRD and RSC predictions using the rectangular geometry is 50.14% (from values in rows 1 and 6) and 50.86% for the traced cross-section geometry (from values in rows 1 and 6). On the other hand, when just the geometry is changed, the greatest PRD from the values in the table is 2.75% (from the E_1 values in row 3, columns 4 and 5). We also see that changes in C_I have a fairly strong effect on the IRD predictions, but not quite as much effect on the RSC predictions: the PRD between the IRD predictions with $C_I = 0.01, 0.03$ is 20.48% for the rectangular geometry (from values in rows 1 and 2, column 4) and 20.56% for the traced cross-section geometry (from values in rows 1 and 2, column 5). On the other hand, for the RSC with $\kappa = 1/10$, the PRD between the predictions made using the rectangular geometry and $C_I = 0.01, 0.03$ (rows 3 and 5, column 4) is only 3.30% and, for the RSC with $\kappa = 1/30$, the PRD between predictions made using the rectangular geometry and $C_I = 0.01, 0.03$ (rows 4 and 6, column 4) is only 0.67%. In addition, when using the traced cross-section geometry, these PRD values for the RSC model are still only 2.72% (for values in rows 3 and 5, column 5) and 0.55% (for values in rows 4 and 6, column 6). The parameter κ appears to have a stronger effect on the RSC predictions than C_I, at least for the range of parameters studied. For example, when $C_I = 0.01$, the PRD between the E_1 predictions in rows 3 and 4, column 4 is 15.33% and for the E_1 predictions in rows 3 and 4, column 5 the PRD is 14.30%. When $C_I = 0.03$, the PRD between the E_1 predictions in rows 5 and 6, column 4 is 12.72% and for the E_1 predictions in rows 5 and 6, column 5 the PRD is 12.14%.

To summarize, we have found that the decision to use the IRD or the RSC model to predict the fiber orientation state has the biggest impact on the predicted elastic modulus of the tensile sample. Secondly, variations in C_I can have a significant influence on predictions made using the IRD model. Thirdly, variations in C_I *do not* have a significant influence on predictions made using the RSC model, but variations in κ do. Fourthly, there is not much change in E_1 predictions when we use our traced cross-section geometry as opposed to the ideal, rectangular geometry. The results for the correlation between the predicted stiffness as a function of the flow parameters C_I and κ are similar to those presented by the authors in their earlier work of [9], whereas the conclusion regarding the bead specific geometry is unique.

3. EXPERIMENTATION

The experimental study consisted of 3D printing strips of composite material with Baylor's LAAM system and cutting two tensile bars out of each strip. Those bars were then tensile tested to determine their elastic modulus.

3.1 Tensile Bar Fabrication

A 13 wt% (~8% volume fraction) carbon fiber filled ABS from PolyOne Corporation was used to print the tensile bars. Each print was two beads wide and three beads tall, and of approximate dimensions 337 mm (13.25") long, 19 mm (0.75") wide, and 9 mm (0.37") thick. Two 152.4 mm (6") tensile bars were cut from each printed strip using a Buehler IsoMet™ Low Speed saw. The extruder temperature zones 1-3 were set to 198 ºC, 204 ºC, and 210 ºC, respectively, and the heated bed was set to 85 ºC. Although the extruder and heated bed temperatures slightly fluctuated during prints, they were watched closely and were never seen to deviate by more than ±4 ºC. The tensile bars sectioned were only taken from a region away from the ends to avoid any edge effects from the extruder as it changed directions.

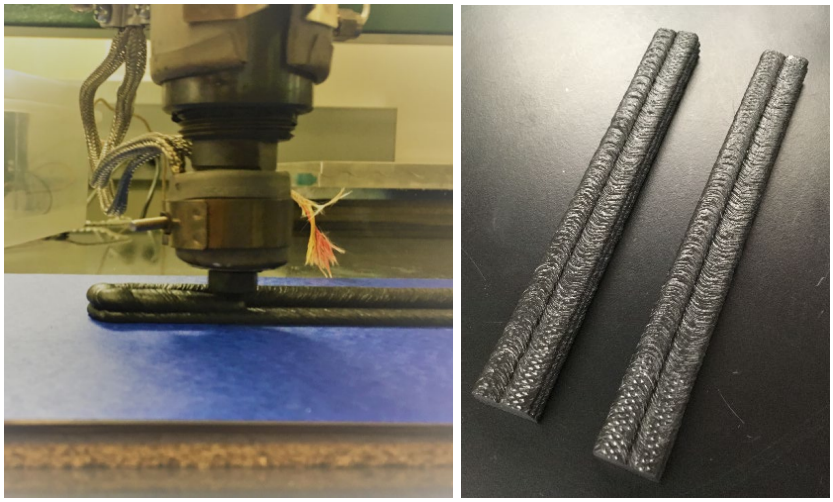


Figure 8. Extruder in mid-print (left; filter was applied to photograph for better lighting) and tensile bars (right).

3.2 Testing Set Up

An MTS QTest/100 machine with a 100 kN load cell was used for tensile testing (see Figure 9). The testing procedure involved a 2 mm/min control rate up to a load of 4000 N, which was below the failure load of a typical tensile bar of around 5-6 kN. An MTS extensometer (Model 634.11F-24) with a gauge length of 25 mm was used and the data acquisition rate for the test was 25 Hz.

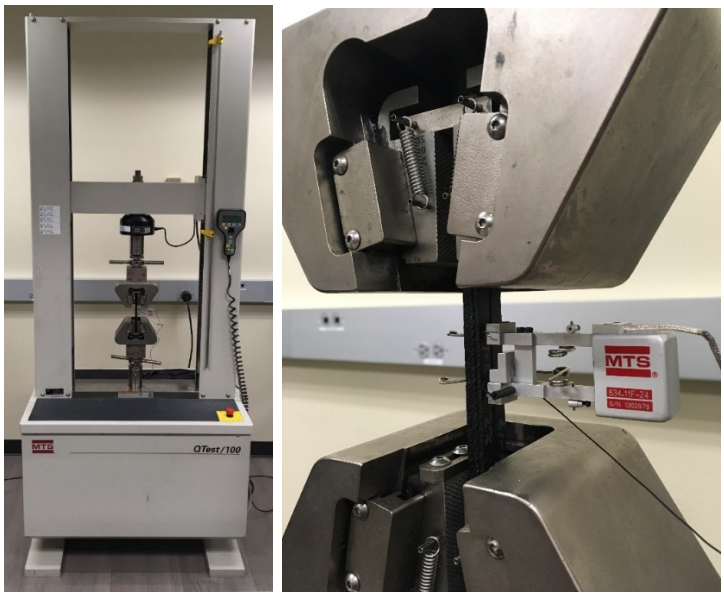


Figure 9. Tensile testing setup: MTS QTest/100 machine with a 100 kN load cell (left) and a MTS extensometer (Model 634.11F-24) with a 25 mm gauge length mounted on a tensile bar (right).

3.3 Testing Results

Data from a typical tensile test is given in Figure 10. To get the stress data for Figure 10, the load data collected from the test was divided by the cross-sectional area of the tensile bar which was found using the tracing method described in subsection 2.3. A linear fit was performed on the initial 50% of the stress-strain curve and the slope of that line was taken to be the elastic modulus. Five tensile tests were performed and analyzed in this way and the results are summarized in Table 3.

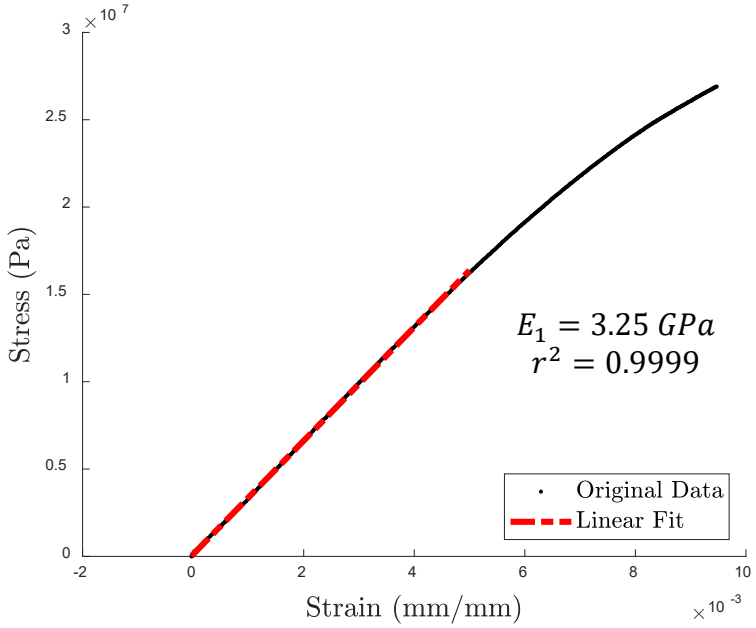


Figure 10. Typical stress-strain curve from a tensile test.

Table 3. Tensile Testing Statistics.

Maximum E_1 (GPa)	Minimum E_1 (GPa)	Mean E_1 (GPa)	Minimum r^2 value of linear fits
3.37	3.20	3.29	0.9997

Upon first glance we see that the E_1 values in Table 3 are over estimated for each of the scenarios investigated and presented in Table 2. In general, the RSC model was more accurate, and the accuracy increased with a decrease in the fiber orientation slowness parameter κ. The most accurate prediction of E_1 was 4.05 GPa which was made using the RSC model with $C_I = 0.03$ and $\kappa = 1/30$ and the traced cross-section geometry. However, this value is still off by 0.76 GPa, or 18.73% in terms of the absolute true percent relative error ($error = |true\ value - predicted\ value|/(true\ value) \times 100\%$). This work is a first pass to compare the experimental with the modeling predictions. Specifically, the actual values for the flow model parameters C_I, κ, and r_e are assumed based on similar studies for injection molded composites. The actual stiffness values for the matrix and fiber is based on internet searches and not from actual testing. Studies are currently underway by the authors to characterize the specific resin and carbon fiber system. Future work should also investigate a coupled model between the local anisotropic viscosity with that of the orientation state. We have observed that for the RSC model, the final orientation state is sensitive to the initial fiber orientation conditions and further studies are warranted to properly characterize the initial conditions.

4. CONCLUSIONS

This paper presents an approach to predict the orientation-state-dependent, effective longitudinal elastic modulus of a short-fiber composite which was 3D printed using the LAAM process. Results are presented for the simplistic assumption of a rectangular extrudate without any voids and for the specific geometry observed in real world samples. We built a LAAM machine and printed several 13 wt% CFF ABS tensile bars for the experimental testing. We used the Isotropic Rotary Diffusion [5] and Reduced Strain Closure [7] fiber orientation models and Tandon and Weng's micromechanics model [11]. We found the RSC model to lead to more accurate predictions of the longitudinal elastic modulus for the model parameters that were considered. Both the IRD and the RSC models for all the parameter combinations that we tried led to over-predictions of the elastic modulus, but predictions within 20% absolute true percent relative error were achieved. Of note is that the use of the deposited bead specific geometry versus a simplified rectangular extruded geometry has very little impact upon the final processed part performance estimation. The largest contributor in properly predicting the part performance is properly characterizing the fiber interaction kinematics coefficients, specifically the interaction coefficient C_I and slowness parameter κ.

5. ACKNOWLEDGEMENTS

The author would like to thank Baylor University for funding this project. Thank you to Dr. Douglas Smith and Blake Heller of Baylor University as well for the use of their flow domain geometry for the die-swell.

6. REFERENCES

[1] Post, B., Richardson, B., Lloyd, P., Love, L., Nolet, S., and Hannan, J., 2017, *Additive Manufacturing of Wind Turbine Molds*, ORNL/TM--2017/290, CRADA/NFE-16-06051, 1376487.

[2] "Shelby Cobra" [Online]. Available: https://web.ornl.gov/sci/manufacturing/shelby/. [Accessed: 20-Jan-2019].

[3] "ORNL 3D-Printed Shelby Cobra," Innovations in Manufacturing [Online]. Available: http://web.ornl.gov/sci/manufacturing/media/news/detroit-show/index.shtml. [Accessed: 03-Feb-2019].

[4] Jeffery George Barker, and Filon Louis Napoleon George, 1922, "The Motion of Ellipsoidal Particles Immersed in a Viscous Fluid," Proceedings of the Royal Society of London. Series A, Containing Papers of a Mathematical and Physical Character, **102**(715), pp. 161–179.

[5] Folgar, F., and Tucker, C. L., 1984, "Orientation Behavior of Fibers in Concentrated Suspensions," Journal of Reinforced Plastics and Composites, **3**(2), pp. 98–119.

[6] Phelps, J. H., and Tucker, C. L., 2009, "An Anisotropic Rotary Diffusion Model for Fiber Orientation in Short- and Long-Fiber Thermoplastics," Journal of Non-Newtonian Fluid Mechanics, **156**(3), pp. 165–176.

[7] Wang, J., O'Gara, J. F., and Tucker, C. L., 2008, "An Objective Model for Slow Orientation Kinetics in Concentrated Fiber Suspensions: Theory and Rheological Evidence," Journal of Rheology, **52**(5), pp. 1179–1200.

[8] Huynh, H. M., 2001, "Improved Fiber Orientation Predictions for Injection-Molded Composites," University of Illinois at Urbana-Champaign.

[9] Russell, T., Heller, B., Jack, D. A., and Smith, D. E., 2018, "Prediction of the Fiber Orientation State and the Resulting Structural and Thermal Properties of Fiber Reinforced Additive Manufactured Composites Fabricated Using the Big Area Additive Manufacturing Process," Journal of Composites Science, **2**(2), p. 26.

[10] Advani, S. G., and Tucker, C. L., 1987, "The Use of Tensors to Describe and Predict Fiber Orientation in Short Fiber Composites," Journal of Rheology, **31**(8), pp. 751–784.

[11] Tandon, G. P., and Weng, G. J., 1984, "The Effect of Aspect Ratio of Inclusions on the Elastic Properties of Unidirectionally Aligned Composites," Polymer Composites, **5**(4), pp. 327–333.

[12] Cintra, J. S., and Tucker, C. L., 1995, "Orthotropic Closure Approximations for Flow-induced Fiber Orientation," Journal of Rheology, **39**(6), pp. 1095–1122.

[13] Verweyst, B. E., and Tucker, C. L., 2002, "Fiber Suspensions in Complex Geometries: Flow/Orientation Coupling," The Canadian Journal of Chemical Engineering, **80**(6), pp. 1093–1106.

[14] "Precision Plasma LLC" [Online]. Available: http://precisionplasmallc.com/. [Accessed: 03-Feb-2019].

[15] "Strangpresse Extruders | Strangpresse."

[16] Heller, B. P., Smith, D. E., and Jack, D. A., "SIMULATION OF PLANAR DEPOSITION POLYMER MELT FLOW AND FIBER ORIENTAITON IN FUSED FILAMENT FABRICATION," p. 16.

[17] Heller, B. P., Smith, D. E., and Jack, D. A., 2016, “Effects of Extrudate Swell and Nozzle Geometry on Fiber Orientation in Fused Filament Fabrication Nozzle Flow,” Additive Manufacturing, **12**, pp. 252–264.
[18] Zhang, D., E. Smith, D., A. Jack, D., and Montgomery-Smith, S., 2011, “Numerical Evaluation of Single Fiber Motion for Short-Fiber-Reinforced Composite Materials Processing,” J. Manuf. Sci. Eng, **133**(5), pp. 051002-051002–9.